A comparative analysis between isotropic and optimization binary diagram influenced by nickel-doping on the $LiMn_2O_4$ spinel type

Kemeridge Malatji[1*], *Regina* Maphanga[2, 3], *and Phuti* Ngoepe[1]

[1]Materials Modelling Centre, University of Limpopo, South Africa
[2] Next Generation Enterprises and Institutions, Council for Scientific and Industrial Research, South Africa
[3]National Institute for Theoretical and Computational Sciences, South Africa

Abstract. The study explores the Ni-rich transition metal as a dopant on the Mn (16d) site of the $LiMn_{1-x}Ni_xO_4$ cathode material. However, lithium manganese oxide is hindered by a limited cycle life, caused by the dissolution of manganese into the electrolyte during electrochemical cycling. Doping lithium-ion battery materials with TM generally enhances their ability to maintain electrochemical capacity over many cycles without compromising the initial reversible capacity at room temperature. This study utilised the genetic algorithm approach and first-principles calculations to investigate the $LiMn_2O_4$ spinel structure. This method identified the most stable phases by simplifying atomic interactions in the $LiMn_2O_4$-$LiNi_2O_4$ system using a series of clusters, which facilitated the corresponding thermodynamic analysis. The comparison and exploration between the full optimized and volume optimized binary calculation was to observe the % difference of the two binary diagrams yielding 13 meV and 1.1 meV, respectively. The two binary ground state diagrams depict the miscibility constituent's behaviour, producing new phases (62 and 77) with different coordinates. The study revealed the five most stable phases at the ground state line, one of which is the opposite ($LiMn_{0.5}Ni_{1.5}O_4$) at X = 0.75 of the high-potential cathode material $LiMn_{0.5}Ni_{1.5}O_4$.

* Corresponding author: kemeridge.malatji@ul.ac.za

1. Introduction

The global demand for alternative energy sources has risen sharply due to the drop of fossil fuels and the considerable ecological harm caused by emissions from motor vehicles [1]. Consequently, there has been a rise in scientific investigations centered on renewable energy and energy storage within the realm of rechargeable lithium batteries, aiming to fulfil the requirements of electric and hybrid electric vehicles(HEVs) [2]. Recent advancements in energy storage research have started to yield results across various types of secondary batteries, with lithium-ion batteries garnering the most attention due to their high energy density and high power density [3]. Promising progress has been made in scientific research on energy storage, leading to outcomes applicable to all secondary battery types [4]. In recent years, there have been numerous efforts to synthesize modified $LiMn_2O_4$ by incorporating different elements, with the goal of inhibiting capacity fading and improving its electrochemical performance. For instance, the general metals Mg [5], Al [6], Ti [7, 8], Cr [9, 10], Fe [11], Co [6, 12, 13], Ni [14], and Cu [15]. The utilization of the doping technique leads to improved electrochemical performance by alleviating the Jahn-Teller effect and enhancing structural stability. Strengthening structural stability and diminishing the Jahn-Teller effect can, in turn, contribute to further advancements in cycle performance. The deployment of MedeA-Universal Cluster Expansion (UNCLE) extends the availability of materials and their corresponding properties at the meso- and microscales. [16] and density functional theory (DFT) code used to calculate the energies for the training-set [17]. The determination of phase stability in the $LiMn_2Ni_2O_4$ ternary spinel system was conducted with a focus on maintaining accuracy, as is typically done in DFT calculations.

In this study, we utilize the cluster expansion technique along with the density functional theory to investigate the characteristics of face-centered-cubic spinel $LiMn_2O_4$ and the Ni-doped $LiMn_{2-x}$ (Ni_x) O_4 ($0<x<2$), employing the cluster expansion formalism. Then, discuss the structures obtained from the fully optimised and isotropic structures from the binary ground state diagrams. Consequently, the diagrams suggest that with an increase in Mn concentrations (x (Mn)>0.5), more structure could be more stable.

2. Method:

Cluster expansion ranks metastable structures according to the formation's enthalpy by autonomously conducting ground state search to navigate through the configuration space. It is crucial to highlight that, atom locations in substitutional doped compounds are well defined inside the crystal lattice, while atom positions in interstitially doped compounds are subject to structural modification. Conversely, in interstitially doped compounds, these positions have the potential to undergo alterations, potentially modifying the overall structure. As a result, the analysis of the stoichiometry of interstitially doped materials becomes challenging when considering the positioning of foreign elements within the crystal structure [18]. To determine the structures and energies of $LiMn_{2-2x}Ni_{2x}O_4$, we performed magnetic density functional theory (DFT) calculations using the Vienna Ab-initio Simulation Package (VASP) [19, 20]. The interaction used in the DFT functional incorporates the generalized gradient approximation (GGA) along with the Perdew, Burke, and Ernzerhof (PBE) functionals for exchange-correlation [19, 21]. The kinetic energy cut-off for the plane wave basis was set at 400 eV, and a Γ-centered Monkhorst-Pack k-point mesh with a uniform spacing of approximately 0.35 $Å^{-1}$ was used for Brillouin-zone integrations. To enhance the convergence of electronic partial occupancies during geometry relaxation, we applied the Methfessel-Paxton order 1 integration method with a smearing width of 0.05 eV and 0.2 eV for the spinel phases generated from the ground state diagram. The utilization of the projector augmented wave (PAW) method allowed for the characterization of frozen atomic cores and

their interactions with valence electrons of the parents phases of $LiMn_2O_4$ and $LiNi_2O_4$. Specifically, the valence electrons, which are the electrons in the outermost shell or energy level of an atom, were identified as $1s^22s^1$ for lithium, $3p^63d^54s^2$ for manganese, $3p^63d^84s^2$ for nickel, and $2s^22p^4$ for oxygen in the parent structures. All computational procedures were conducted within the MedeA® software environment [22].

The genetic algorithms approach operates based on the principle that any characteristic of a crystal, influenced by the arrangement of atoms at specific sites (configuration), can be expanded using polynomials of fundamental functions for each site. The crucial assumption here is that the contribution of free energy from other degrees of freedom (for example, vibrational and magnetic) is small and coarse-grained. As illustrated in the equation below, the physical property of the structure, which depends on the atomic configuration, can be expressed as a sum of spin products.

$$E(\sigma) = J_0 + \sum_i J_i S_i + \sum_{i<j} J_{ij} S_i S_j + \sum_{i<j<k} J_{ijk} S_i S_j S_k + \cdots \quad (1)$$

The parameters J_i are known as effective cluster interactions (ECI) and have the same dimension as the expanded property. J_0 stands for the null figure, which serves as a constant value. The enthalpy of formation is more suitable for fitting and determining the optimal set of values because they have to reach a minimum. The ECI is independent of the configuration σ and contains the properties of the figures determined by the spin products. In practical applications, significantly truncated expansions provide essentially identical results, rendering the method practical and, consequently, valuable in a range of situations [16], where the typical values for the accuracy of the fit are a few meV per atom.

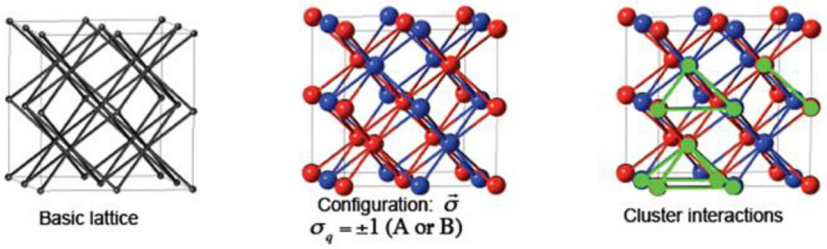

Fig. 1. The diagram represents a fundamental lattice comprising atoms of different types, denoted as A and B. These atoms are arranged to create the favourable phases, forming a periodic ordering of A and B atoms. In this context, a pseudo spin operator denoted as $\vec{\sigma} = \pm 1$ takes on values of ±1. Specifically, it assumes a value of +1 when describing the configuration where atom A occupies site q, and a value of -1 when atom A is replaced by atom B at that site.

This aims to identify and study mixed crystal phases and organise metastable phases by considering the enthalpy of formation. Throughout this process, it maintains the prognostic capability and the validity associated with first-principles density functional methods. Ternary systems (or binary systems with vacancies) e.g. Refs, [18,20] are still rather scarce because of the effort needed. The present work focuses on the modelling of a ternary system ($(LiNiMnO_4)_8$) based on a body centred cubic lattice for full optimization. Although elemental manganese (Mn) and nickel (Ni) crystallize in a face-centered cubic lattice, cluster expansion did not take into account FCC structures and similar structures. We made this decision based on the primary focus of this study, which centers on the nickel-doped spinel structure. It generated a multitude of configurations with changing doped nickel and symmetries using the phase diagram of the ground state. The iterations persist till all energies

of the structures surpass the energy computed for the linear ground state structure at each measured concentration and align with the predictions made by the cluster expansion.

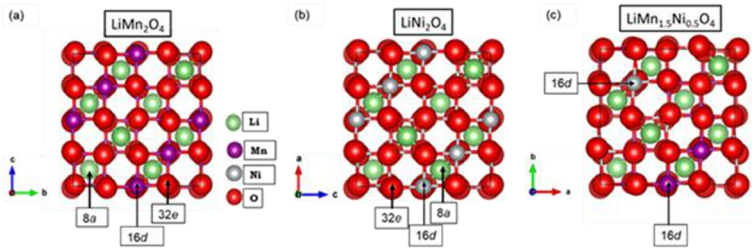

Fig. 2. (a) Exhibits the $LiMn_2O_4$ spinel structure with a consistent distance between unit cells in the crystal lattice, where a = 8.120 Å, in contrast to **Fig. 2** (b) arrays $LiNi_2O_4$ spinel composition show casing a lattice constant of a = 8.046 Å. At the 32e sites, the oxygen atoms within the unit cell, which possesses the full symmetry of the spinel lattice, arrange themselves in a face-centered-cubic structure. Li atoms occupy the tetrahedral (8a) cation sites, while Mn cations fill the octahedral (16d) sites. In the assessed arrangement range for each Nickel content, Nickel occupies the octahedral 16d sites, as shown in **Fig. 2** (c), with consistent distances between unit cells in the crystal lattice, where a =9.868, b =16.75, c =5.697 [23].

3. Results and Discussion

Figure 3 and 4 are the results of $LiMn_2Ni_2O_4$ where the flowchart was set with the same parameters but differed in that one was isotropic, and the other was fully optimized.

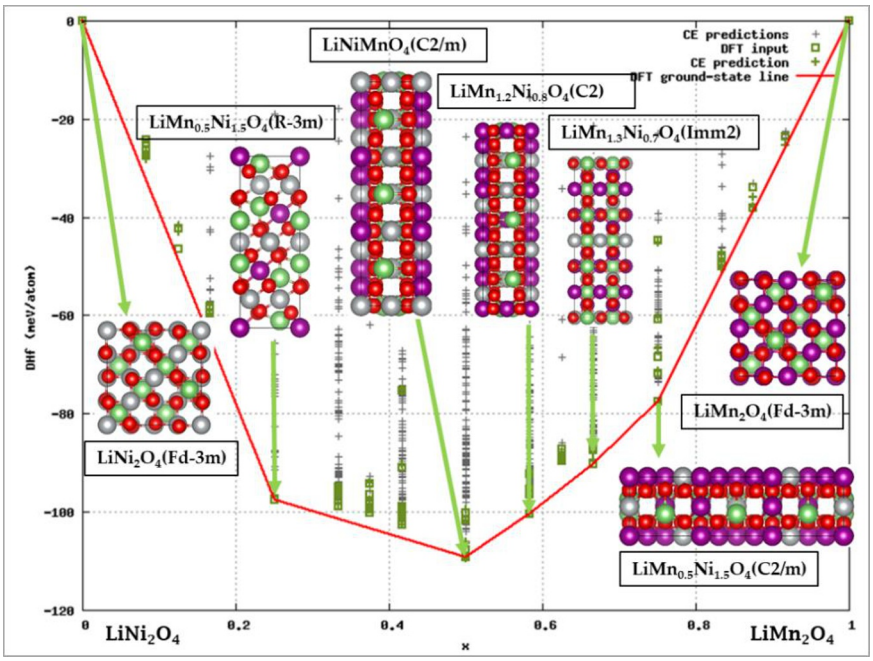

Fig. 3. A quaternary isotropic volume system, composed of mixed Ni and Mn components, simplifying atomic interactions in the $LiMn_2O_4$-$LiNi_2O_4$ system using a series of clusters, thereby facilitating the associated thermodynamic analysis.

A quaternary isotropic volume system in Figure 3 illustrates an isotropic-only volume optimization binary ground state diagram featuring an un-ordered structure. As an alternative to a comprehensive

structural optimization, we opted for isotropic volume optimization, wherein both minimization stages involve isotropic volume optimization. To address anomalies in DFT total energy values, we improved the VASP flowchart's accuracy. This involved elevating the plane wave cut-off energy from 300 - 400 eV in the optimization cluster expansion step and reducing the spacing k-points from 0.5 to 0.35 1/Ang of the second minimization step. The result of the isotropic generalized gradient approximation flowchart and the optimization calculation unveiled miscible constituents, as illustrated in Figure 3. This implies that phases generated in proximity to the ground state line, exhibiting the lowest enthalpy of formation at a given concentration, should be stable. Thermodynamically stable structures are shown by the solid curved line, which is the ground-state line as established by DFT analysis. After predicting all the structures' energies, there were 62 new stable-generated phases, of which only six were considered sturdier. The sturdy phases derived from the schematic in plot 3 possesses various formation enthalpies, symmetries, cell parameters, and atomic positions within the crystal that are similar. In addition, Figure 3 yielded a value of 1.1 meV less than the standard value 5 meV per active position, indicating how well the energies of the structures in the drill differentiate with one another and the robust nature of cluster expansion.

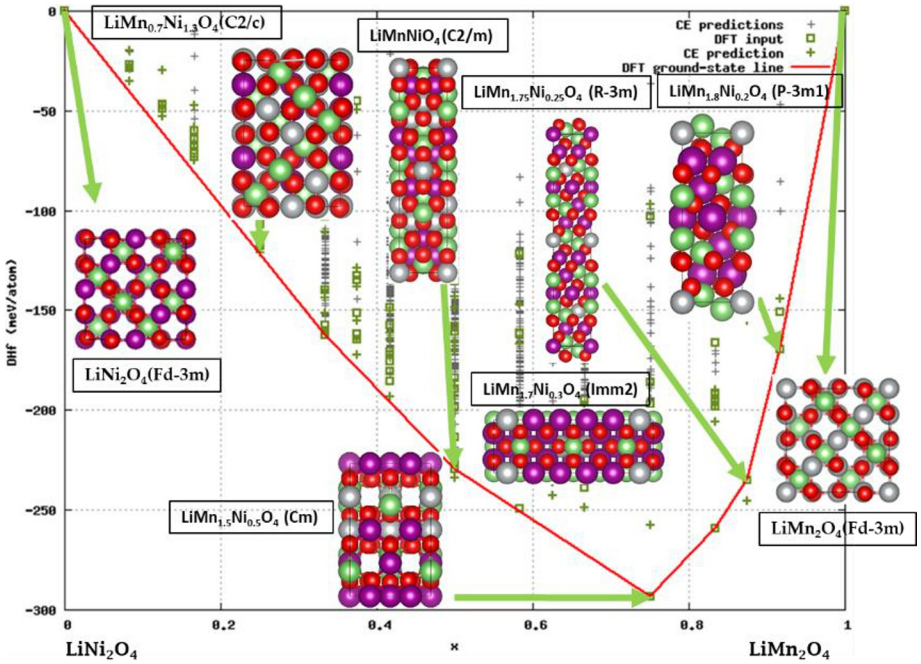

Fig. 4. A quaternary system, featuring relaxed atomic positions, and changes in cell shape and volume, composed of mixed Ni and Mn components with ordered phases, has a converged genetic algorithm with no new phases below the DFT-based ground state line at 0K.

The quaternary system above illustrates a completely optimized binary diagram with atom relaxation, allowance for changes in volume, and the flexibility of cell shape and the structure remaining non-magnetic and un-ordered. The comprehensive optimization shows that of the 77 new structures generated by the binary ground state diagram, only eight (8) are

stable. Consistent with the parameters employed in Figure 3, the optimization cluster expansion stage used the same plane-wave basis cut-off, increased from 300 to 400 eV, and reduced the spacing between k-points from 0.5 to 0.35 in the second minimization stage. The miscible constituents depicted in Figure 4's schematic suggest that the phases that are formed near the ground states are the most favourable phases with the lowest enthalpy of formation at a given x-values. The red line denotes thermodynamically stable structures and represents the ground-state line determined by DFT analysis. In Figure 4, stable structures demonstrate that space groups in Figure 2 at x = 0.5 and 0.75, possess different consistent distance between unit cells in the crystal lattice, maintaining the same Wyckoff positions, and exhibit distinct energies of formation. However, the completely optimized computation resulted in a cross-validation score of 13 meV, indicating a suboptimal cluster expansion with a CVS exceeding 5 meV per active position. Consequently, structures from the diagram in Figure 4 are not considered due to the elevated CVS being greater than the standard value of 5 meV. This increased error may be attributed to value of the Mn content in comparison to the isotropically optimized diagram if Figure 4. Thus, the concentration of Mn must be restricted to the occupancy of 0.8.

Table 1. The lattice parameters, formation enthalpies, and volumes of the most favourably generated phase (7) at various x-concentrations.

X(Mn)-Concentration	Stable Structures	Lattice Parameters (Å)	Energy of formation ΔH_f(kJ/mol)	Volume (Å)
0	$LiNi_2O_4$	a=b=c=8.120	-743.78	535.42
0.25	$LiMn_{0.5}Ni_{1.5}O_4$	a=9.507, b= 5.8, c=13.915	-938.59	786.77
0.5	$LiMnNiO_4$	a=b=5.766≠, c=13.915	-1680.07	400.64
0.58	$LiMn_{1.2}Ni_{0.8}O_4$	a=9.550, b=17.357, c =5.792	-5773.33	780.97
0.69	$LiMn_{1.3}Ni_{0.7}O_4$	a=17.481, b=5.807, c=7.614	-2968.22	773.03
0.75	$LiMn_{1.5}Ni_{0.5}O_4$	a =9.868, b =16.750, c =5.697	-2014.03	786.05
1	$LiMn_2O_4$	a=b=c=8.046	-1055.37	520.84

Table 1 presents all structures on the DFT ground state line ($LiMnNiO_4$, $LiMn_{1.2}Ni_{0.8}O_4$, $LiMn_{1.3}Ni_{0.7}O_4$, $LiMn_{1.5}Ni_{0.5}O_4$) derived from a binary diagram with a lower cross-validation score (CVS) of 1.1 MeV. Notably, $LiMn_{1.2}Ni_{0.8}O_4$, $LiMn_{1.3}Ni_{0.7}O_4$, $LiMn_{1.5}Ni_{0.5}O_4$, and $LiMnNiO_4$ exhibit lower energies in comparison to other structures, primarily attributed to the reduced nickel content. Analysing the parent structures at x = 0 ($LiNi_2O_4$) and x = 1 ($LiMn_2O_4$) reveals the influence of Ni-doping during the cluster expansion random mixing. The formation energy of -1055.37 kJ/mol for $LiMn_2O_4$ is notably more stable than the -743.78 kJ/mol of the layered Ni-rich structure ($LiNi_2O_4$). This validates the function of the Mn-content in stabilizing other structures. The isotropically optimized binary diagram predicted a number of cathode materials with compositions such as $LiMn_{0.5}Ni_{1.5}O_4$ and $LiMn_{1.5}Ni_{0.5}O_4$, as detailed in Table 1. These predictions align with both theoretical and experimental findings from previous studies[18, 23, 24].

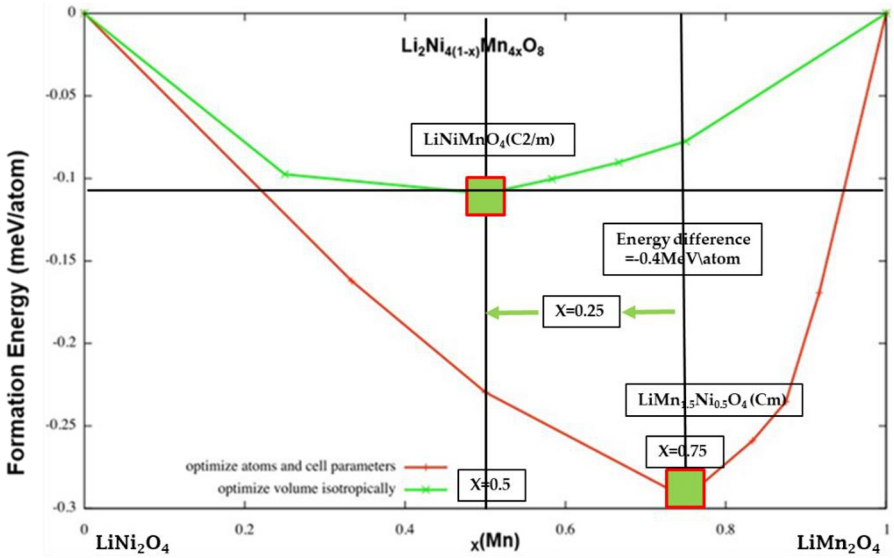

Fig. 5. Highlights of the differences in optimization approaches of the fully optimized diagram accounts for both atomic positions and cell shape changes, while the isotropically optimized version focuses solely on uniform volume adjustments without altering cell shape.

The formation energy comparison of the DFT ground-state lines for a quaternary system with relaxed atomic positions, as well as changes in cell shape and volume, and a quaternary isotropic volume, are significantly illustrated in the plot above. The substantial change in formation energy shown in Figure. 5 suggests that the position of the oxygen atom might be influencing this variation. This suggests the possibility that another phase might be more favourably stable at concentrations where (x Mn) is greater than 0.5. The comparison of the leave-one-out cvs for the quaternary isotropic volume produced a magnitude of 1.1 meV which is less than the quaternary system with relaxed atom positions, shape and volume cell change, equal to 13 meV and greater than the standard value of 5 meV. The accuracy of the CE models outcomes depended on the quality of the cluster functions and coefficients. It might not capture all types of interactions, especially in highly disordered systems. Therefore the high cvs becomes unreliable measure to predict or show the accuracy which suggests that the structural stability is not correctly predicted.

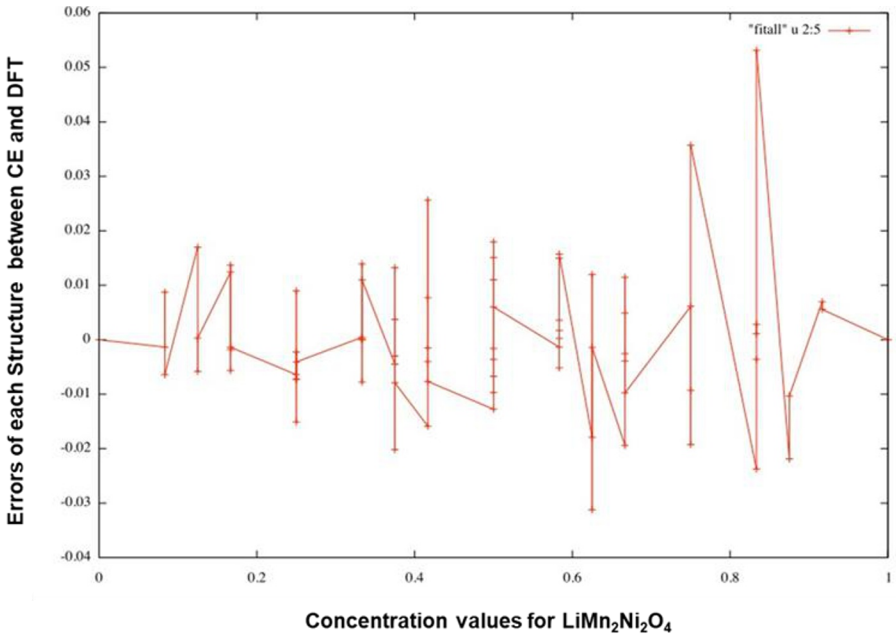

Fig. 6. The errors of each structure between the CE prediction and the DFT inputs at each concentration of $LiMn_2Ni_2O_4$ during a fully optimised genetic algorithm flowchart.

Figure 6 shows the errors of a fully optimised binary ground state diagram of $(LiNi_2Mn_2O_4)_8$ between cluster expansion and DFT. The figure displays the errors of each compositions energy of the nickel and manganese content. By assessing the energy of different configurations, CE helped in optimizing $(LiNi_2Mn_2O_4)_8$ formation energy However, significant changes in energy due to variations in atomic positions and cell parameters introduced uncertainty that the cluster expansion cannot accurately predict. When the cvs values is below the standard cvs then a good cluster expansion results are achieved, where then various properties such as the formation energy for the favourable sturdy composition on the DFT ground state line can be calculated. By using this process, the genetic algorithm facilitates the identification and examination of favourable phases on the ground-state phases. Analysing the results the concentration range failed to lower the final CVS from 13 -12 meV/atom. Therefore, the best next step in this study was to use the isotropically optimised binary ground state diagram to calculate the properties of the new favourable structures. However, based on high values of CVS after relaxations and errors of each structure between cluster expansion and DFT as shown in Figure 6, it would be trivial to perform Monte Carlo simulation as all summarised errors by the CVS will be transferred to the Monte Carlo simulations.

4. Conclusion

The cluster expansion formalism, as implemented in the UNCLE code, was used to investigate nickel-doped LMO phase stability. The ground-state phase diagram produced a variety of structures with varying concentrations and symmetries. The cross-validation scores for the isotropically volume-optimized and fully-optimized structures were 1.1 meV and 13 meV, respectively, indicating good and bad cluster expansion. A total of 704 structures provided a well converged cluster expansion for a very complex system spinel $LiMn_2O_4$, was successfully investigated using DFT methods. Ground state energy structures (about 6 stable

structures) were identified with regard to the ground-state line and the most stable structures is $LiMn_2Ni_2O_4$ of which it is corresponding to the lowest Heats of Formation.
With complete structural optimization (atomic and cell parameters) and isotropic volume optimization, there is a significant energy difference between the two ground state lines. Nickel doping helps improve the structural stability by reducing the dissolution of Mn, as Ni ions stabilize the crystal lattice. As shown by the variations in formation energies in the graphs and the table, the impact of nickel incorporation into the $LiMn_2O_4$ structure is evident. Furthermore, the graphs suggest the potential stability of other structures at higher Mn concentrations (x (Mn) > 0.5) in relation to the isotropic diagram. The isotropic calculation confirmed that the set-up of the structure to perform according to the standard cvs value criteria would have been different under the full optimisation. Therefore it would be advisable to further perform geometry optimisation calculations before utilising the generated phases.

The authors acknowledge the Centre for High-Performance Computing (CHPC) in Cape Town and the Materials Modelling Centre (MMC) at the University of Limpopo for providing the computational resources essential for this work. The financial support from the National Research Foundation (NRF) is also acknowledged and greatly appreciated. The Materials design and Dr David Reith from Materials design.

References

1. M. Höök, X. Tang, Energy policy **52**, 797-809 (2013)
2. A. Yamada, S. C. Chung, K. Hinokuma, J. Electrochem. Soc. **148**, A224 **(**2001)
3. L. Lu, X. Han, J. Li, J. Hua, M. Ouyang, J. Power Sources **226**, 272-288 (2013)
4. J.W. Fergus, J. Power Sources **195**, 939-954 (2010)
5. Singh, P.; Sil, A.; Nath, M.; Ray, S, Ceram. -Silik **54**, 38-46 (2010)
6. F.A. Amaral, N. Bocchi, R.F. Brocenschi, S.R. Biaggio, R.C. Rocha-Filho, J. Power Sources **195,** 3293-3301 **(**2010|)
7. D.Q. Liu, X.Q. Liu, Z.Z. He, Mater. Chem. Phys. **105** 362-366 (2007)
8. Z. Peng, Q. Jiang, K. Du, W. Wang, G. Hu, Y. Liu, J. Alloys Compd. **493**, 640-644 (2010)
9. W. Xu, A. Yuan, L. Tian, Y. Wang, J. Appl. Electrochem.,**41**, 453-460 (2011)
10. P. Singh, A. Sil, M. Nath, S. Ray, Adv. Mater. Res. **67**, 233-238 (2009)
11. Q. Luo, A. Manthiram, J. Electrochem. Soc. **156**, A84 (2008)
12. A. Sakunthala, M. Reddy, S. Selvasekarapandian, B. Chowdari, P.C. Selvin, Electrochim. Acta **55**, 4441-4450 (2010)
13. A.Y. Shenouda, E.S.M. El Sayed, H.K. Liu, J. New Mater. Electrochem. Syst **14**, 19-26 **(**2011)
14. H. Wu, J. Tu, X. Chen, Y. Li, X. Zhao, G. Cao, J Solid State Electrochem **11**, 173-176 (2007)
15. Y. Ein-Eli, R. Urian, W. Wen, S. Mukerjee, Electrochim. Acta **50**, 1931-1937 (2005)
16. D. Lerch, O. Wieckhorst, G.L. Hart, R.W. Forcade, S. Müller, Model. Simul. Mat. Sci. Eng. **17**, 055003 (2009)
17. A. Van der Ven, G. Ceder, Phys. Rev. B **71**, 054102 (2005)

18. K. Gurkin, Investigation of Material Composite Li3V2 (PO4) 3 with $LiMn_{2-x}Ni_xO_4$ for. Northeastern University Boston (2010)
19. G. Kresse, J. Furthmüller, Phys. Rev. B, **54** 11169 (1996)
20. J.P. Perdew, A. Ruzsinszky, G.I. Csonka, O.A. Vydrov, G.E. Scuseria, L.A. Constantin, X. Zhou, K. Burke, Phys. Rev. Lett. **100**, 136406 (2008)
21. G. Kresse and J. Furthmüller, Comput. Mat. Sci. **6**, 15 (1996).
22. P.R. Alonso, G.H. Rubiolo, Phys. Rev. B 62, 237 (2000)
23. K.T. Malatji, D. Santos-Carballal, U. Terranova, P.E. Ngoepe, N.H. de Leeuw, S. Afr. J. Sci. **74**, 3–7 (2021)
24. A. Van der Ven, G. Ceder, Phys. Rev. B **71**, 054102 (2005)